

RESEARCH ARTICLE | NOVEMBER 10 2022

Numerical investigation of the segregation of turbulent emulsions

T. Trummler ; A. Begemann ; E. Trautner ; M. Klein 



Physics of Fluids 34, 113324 (2022)

<https://doi.org/10.1063/5.0112565>



CrossMark

AIP Advances

Why Publish With Us?

-  **25 DAYS**
average time to 1st decision
-  **740+ DOWNLOADS**
average per article
-  **INCLUSIVE**
scope

[Learn More](#)

Numerical investigation of the segregation of turbulent emulsions

Cite as: Phys. Fluids **34**, 113324 (2022); doi: 10.1063/5.0112565

Submitted: 21 July 2022 · Accepted: 26 October 2022 ·

Published Online: 10 November 2022



View Online



Export Citation



CrossMark

T. Trummler,^{a)} A. Begemann, E. Trautner, and M. Klein

AFFILIATIONS

Institute of Applied Mathematics and Scientific Computing, Bundeswehr University Munich Werner-Heisenberg-Weg 39, 85577 Neubiberg, Germany

^{a)} Author to whom correspondence should be addressed: theresa.trummler@unibw.de

ABSTRACT

We study the segregation of emulsions in decaying turbulence using direct numerical simulations in combination with the volume of fluid method. To this end, we generate emulsions in forced homogeneous isotropic turbulence and then turn the forcing off and activate the gravitational acceleration. This allows us to study the segregation process in decaying turbulence and under gravity. We consider non-isodensity emulsions, where the dispersed phase is the lighter one. The segregation process is driven by both the minimization of the potential energy achieved by the sinking of the heavier phase as well as the minimization of the surface energy achieved by coalescence. To study these two processes and their impacts on the segregation progress in detail, we consider different buoyancy forces and surface tension coefficients in our investigation, resulting in five different configurations. The surface tension coefficient also alters the droplet size distribution of the emulsion. Using the three-dimensional simulation results and the monitored data, we analyze the driving mechanisms and their impact on the segregation progress in detail. We propose a dimensionless number that reflects the energy release dominating the segregation. Moreover, we evaluate the time required for the rise of the lighter phase and study correlations with the varied parameters: gravitational acceleration and surface tension coefficient.

© 2022 Author(s). All article content, except where otherwise noted, is licensed under a Creative Commons Attribution (CC BY) license (<http://creativecommons.org/licenses/by/4.0/>). <https://doi.org/10.1063/5.0112565>

I. INTRODUCTION

Emulsions are suspensions of immiscible liquids (such as oil and water) and play a central role in a wide range of industrial processes, such as food processing,^{1–3} pharmaceutical processes,⁴ and oil production.^{5,6} Moreover, current research is examining the application of fuel–water emulsions for more efficient and environmentally friendly power generation. Examples include gasoline–water direct injection (GWDI) for future gasoline engines^{7,8} or fuel–water emulsions for small gas turbines⁹ and diesel engines.¹⁰ In particular, for power generation applications, better understanding of the stability of emulsions and the timescale of the segregation process is of central importance. To this end, we numerically study the segregation of emulsions in decaying turbulence under gravity.

The formation of an emulsion requires energy input in the form of kinetic energy to deform and breakup droplets. For a non-isodensity emulsion, the mixing of the lighter and the heavier phase requires additional energy input. In order to keep an emulsion stable, a continuous supply of energy is then required. Without further energy input, emulsions are unstable due to the natural tendency to minimize

the potential and surface energy. To minimize the net potential energy, the heavier phase sinks, which is governed by the gravitational acceleration g and the density difference between the two phases. To minimize the surface energy, the droplets coalesce, thus reducing the interface area. A higher surface tension σ leads to a higher variation in the surface energy and, thus, increases the tendency for coalescence. Furthermore, it should be noted that interface minimization can be prevented by the presence of surfactants,^{11,12} such as the naturally occurring surfactants, e.g., asphaltene and resins. Both rising and coalescence lead to the segregation of emulsions, which can be quantified by the height of the lighter phase, i.e., the position of its center of mass in the direction of the gravitational acceleration, and the interface area, respectively. However, the two processes of rising and coalescence mutually interact with each other since the larger droplets rise more easily, and acceleration in one direction promotes coalescence.

Experimental studies on the segregation process of emulsions mainly focus on chemical engineering aspects and monitor the height of the coalescing interface. There are several studies in the literature related to modeling of gravity assisted oil–water emulsion separation

in oil production processes.^{13–19} The proposed models are designed for gravity settlers to separate the water during the oil production process and deliver correlations for the temporal evolution of zone heights. A review of these models is provided by Frising *et al.*²⁰ Most of these models require various input and modeling parameters and are very sophisticated. Furthermore, limited optical access makes experimental studies of emulsion segregation processes challenging and requires advanced measurement techniques.²¹ For this reason, information on the interface area in segregating the emulsions is hard to access. In this work, we want to complement these experimental studies with a numerical investigation for a generic configuration.

Several numerical studies of emulsions and emulsification processes have been reported in the past, mostly focusing on droplet size distributions. First numerical emulsion studies employed lattice-Boltzmann (LB) methods, e.g., Perlekar *et al.*,²² Skartlien *et al.*,²³ and Mukherjee *et al.*²⁴ More recently, Cialesi-Esposito *et al.*²⁵ and Begemann *et al.*²⁶ utilized direct numerical simulations (DNS) combined with the volume of fluid (VOF) method for these investigations. Moreover, several numerical studies, such as Komrakova²⁷ and Shao *et al.*,²⁸ focused specifically on the breakup of droplets. The reverse process to emulsification, namely, coalescence and rising of the lighter phase, was studied in the following papers: Dodd and Ferrante²⁹ investigated droplet coalescence and the droplet–turbulence interaction in decaying turbulence and found that the energy release due to coalescence processes has an impact on the decay of the turbulent kinetic energy.

An important and central aspect of multiphase configurations is the effect of the buoyancy force due to a density difference between the phases and gravity. Previous numerical studies on the effect of the buoyancy force considered, for example, bubble-laden downflow configurations^{30–32} or rising bubbles.^{33,34} In addition, Saeedipour *et al.*³⁵ and Estivaleres *et al.*³⁶ have recently performed simulations of the phase inversion test case, where the lighter phase is initialized at the bottom of a box and rises due to gravitational acceleration. Despite the central importance of the buoyancy force on the segregation of non-iso-density emulsions, we are not aware of any previous numerical simulation studies on this. The effect of the buoyancy force on emulsion stability and emulsion segregation is of particular importance for various applications, especially with respect to the emulsions in power generation (see above). With this work, we aim to complement experimental studies^{37,38} with numerical investigations of emulsion stability and segregation. CFD simulations can overcome some of the limitations and challenges in experimentally characterizing emulsions^{21,39} and provide new and more detailed insight.

This work builds upon our recent paper on emulsification and emulsions.²⁶ Using the enhanced linear forcing approach proposed in our recent paper, we can generate a statistically stationary emulsion with a prescribed turbulent kinetic energy and therewith obtain well-defined initial conditions for studying the segregation. In this work, we study the segregation of emulsions resembling oil-in-water liquid-liquid emulsions in terms of density ratio. In our study, we vary the buoyancy force (by varying the gravitational acceleration g) and the surface tension coefficient σ , the latter resulting in different droplet size distributions of the emulsions. Hence, we focus on the parameters affecting the segregation progress (minimization of the potential and surface energy). For our studies, we use DNS with the finite volume approach and the VOF method. The emulsions are generated by a

linear forcing of turbulence augmented with a PID controller.²⁶ We then switch off the forcing and activate the gravitational acceleration and let the emulsions segregate in decaying turbulence under gravity.

This paper is structured as follows. In Sec. II, we describe the computational method. Section III presents the considered configurations and the numerical setup. The results are presented in Sec. IV, which first studies the segregation process in detail and then focuses on the energy releases to elucidate the dominant mechanisms and finally studies the timescale of the segregation. Section V summarizes the findings and draws conclusions.

II. COMPUTATIONAL METHOD

The simulations are conducted with the open source code PARIS (PARallel, Robust, Interface Simulator).⁴⁰ PARIS has been specifically designed for simulations of multiphase flows and is often used for studies of atomization processes, see, e.g., Refs. 41–44, as well as other multiphase flow configurations.³⁴

The solver uses the single fluid formulation⁴⁵ of the incompressible Navier–Stokes equations. The continuity and momentum equations are given as follows:

$$\frac{\partial u_i}{\partial x_i} = 0, \quad (1)$$

$$\rho \left(\frac{\partial u_i}{\partial t} + \frac{\partial u_i u_j}{\partial x_j} \right) = -\frac{\partial p}{\partial x_i} + \frac{\partial}{\partial x_j} \left[\mu \left(\frac{\partial u_i}{\partial x_j} + \frac{\partial u_j}{\partial x_i} \right) \right] + \sigma n_i \kappa \delta_s + \rho g_i, \quad (2)$$

with the density ρ , the dynamic viscosity μ , the i^{th} velocity component u_i , the pressure p , and the gravitational acceleration g_i . In each cell, the density and viscosity values are linearly interpolated using the local volume fraction α of the dispersed phase, which is tracked with the geometrical VOF method:⁴⁶

$$\rho = \alpha \rho_d + (1 - \alpha) \rho_c, \quad \mu = \alpha \mu_d + (1 - \alpha) \mu_c. \quad (3)$$

The subscripts d and c denote the dispersed and the carrier phase, respectively.

The Continuous-Surface-Force (CSF) approach⁴⁷ determines the surface tension force from the surface tension coefficient σ , the interface normal $n_i = \frac{\partial \alpha}{\partial x_i} / |\nabla \alpha|$, the interface indicator function $\delta_s = |\nabla \alpha|$, and the interface curvature $\kappa = \frac{\partial n_i}{\partial x_i}$. The latter is accurately computed using a state-of-the-art height function approach.⁴⁸ Details on its implementation in PARIS can be found in Aniszewski *et al.*⁴⁰

The advection of the VOF marker function is performed using a geometrical interface reconstruction algorithm. The respective transport equation is given as follows:

$$\frac{\partial \alpha}{\partial t} + u_i \frac{\partial \alpha}{\partial x_i} = 0, \quad \alpha = \begin{cases} 1, & \text{if } \mathbf{x} \text{ is in dispersed phase,} \\ 0, & \text{if } \mathbf{x} \text{ is in carrier phase.} \end{cases} \quad (4)$$

A red-black Gauss–Seidel solver with overrelaxation is employed to solve the Poisson equation for pressure in the framework of the projection method. The simulation is advanced in time using a second-order predictor-corrector method. For the spatial discretization, the finite-volume approach is realized using a cubic grid. The velocity components are stored on a staggered grid, while the pressure and the VOF marker function, as well as the local densities and the viscosities resulting from the latter, are computed at the cell centers. The third-order

Quadratic Upstream Interpolation for Convective Kinematics (QUICK) scheme⁴⁹ has been chosen to discretize the convective term of the momentum equation, while its viscous term is treated using second order accurate central differences.

To generate a turbulent emulsion in homogeneous isotropic turbulence (HIT), we employ the linear Lundgren forcing⁵⁰ extended by a PID controller; see Begemann *et al.*²⁶ This extension provides a constant turbulent kinetic energy and accelerates the emulsification process.

III. CONSIDERED CONFIGURATIONS

In this paper, we study the segregation of emulsions under different buoyancy forces obtained by varying the gravitational acceleration g . Furthermore, we also consider the emulsions with different droplet size distributions, which are obtained by a variation in the surface tension coefficient σ .

Emulsions feature polydisperse droplet size distributions. A reference value for the droplet size distributions in the emulsions is given by the Hinze scale d_H ,⁵¹ which is expected to be the most stable maximum droplet diameter in the emulsions for HIT. d_H is determined by

$$d_H = (We_{d,crit}/2)^{3/5} (\rho_c/\sigma)^{-3/5} \varepsilon^{-2/5}, \quad (5)$$

where $We_{d,crit}$ denotes the critical droplet Weber number, for which we assume $We_{d,crit} = 1.17$ following Hinze⁵¹ and recent numerical studies.^{24,25} Moreover, ρ_c is the density of the carrier fluid, σ is the surface tension coefficient, and ε is the dissipation rate associated with the turbulence intensity.

For emulsions, a Weber number We_l using a characteristic length scale can be defined as

$$We_l = \frac{\rho_c u'^2 l}{\sigma}, \quad (6)$$

taking into account the effect of surface tension. In experimental studies (e.g., Ref. 22), for example, the diameter of the stirrer is used as the length scale. For the HIT considered here, the integral length scale of the turbulent flow field is employed. Therefore, the emulsions at a stationary state can be characterized by We_l as demonstrated and discussed in Begemann *et al.*²⁶ Moreover, using $l = (u'^2)^{3/2}/\varepsilon$, the correlation

$$d_H/l \propto We_l^{-3/5} \quad (7)$$

is obtained.

The emulsions are generated in HIT with a constant turbulent kinetic energy k . For isotropic turbulence, k is given by $k = (3/2)u'^2$, where u' denotes the velocity fluctuation. In the case of linear forcing, the dissipation rate ε is determined by k and the integral length scale l , which is 20% of the domain length,^{52,53} using the correlation $l = (u'^2)^{3/2}/\varepsilon$. Additionally, for HIT, a characteristic dimensionless number is the Taylor Reynolds number $Re_\lambda = \lambda u'/\nu$ formed with the Taylor micro-scale $\lambda = \sqrt{15\nu/\varepsilon}u'$.

We simulate five different configurations. The parameters common for all configurations are summarized in Table I. The volume fraction of the dispersed phase is $\phi = V_d/(V_d + V_c) = 1/8$ for all cases. The carrier and dispersed fluid have a density of $\rho_c = 1$ and $\rho_d = 0.9 \text{ kg/m}^3$, respectively, thus making the dispersed fluid the lighter one. The kinematic viscosities are both set to

TABLE I. Constant emulsion parameters.

ϕ (-)	ρ_c (kg/m ³)	ρ_d (kg/m ³)	$\nu_c = \nu_d$ (m ² /s)	k (m ² /s ²)	ε (m ² /s ³)	Re_λ (-)	L (m)	N (-)
1/8	1	0.9	0.001	0.5	0.153	104	2π	384

$\nu_d = \nu_c = 0.001 \text{ m}^2/\text{s}$. We here study the emulsions generated at a turbulence intensity of $k = 0.5 \text{ m}^2/\text{s}^2$ in a cubic domain with length $L = 2\pi$ and, thus, a Taylor Reynolds number of $Re_\lambda = 104$ and a dissipation rate of $\varepsilon = 0.153 \text{ m}^2/\text{s}^3$. We discretize the domain with $N = 384$ cells in each direction ($\approx 57 \times 10^6$ cells in total). This grid resolution has been chosen to fulfill the criterion $K_{max}\eta \geq 1.5$, see, e.g., Pope,⁵⁴ where K_{max} is the maximum wavenumber $K_{max} = N\pi/L$, and η is the Kolmogorov scale $\eta = (\nu^3/\varepsilon)^{1/4}$, given by the kinematic viscosity ν and the dissipation rate ε . A grid study of this configuration can be found in our recent paper.²⁶

For the simulation of the segregation process, first, turbulent emulsions in HIT are generated as described in detail in Begemann *et al.*²⁶ We consider a cubic box with periodic boundary conditions. In order to generate turbulent emulsions, we first perform single-phase simulations to obtain a fully developed single-phase HIT. Then, we initialize the dispersed phase as spherical droplets, which breakup in the linearly forced HIT, and an emulsion is obtained as visualized in Fig. 1(a). At a statistically stationary state, we turn the forcing off and prescribe slip walls in the direction of the gravitational force; see Fig. 1(b). A thin layer (four cells) of the carrier fluid is additionally initialized at the bottom to detach dispersed structures there. Then, we let the emulsions segregate [Fig. 1(c)]. The time t is measured from the time instant when the forcing is turned off.

Table II lists the considered configurations for the segregation. The configurations are adopted from our previous investigation²⁶ of emulsification processes and the emulsions at the statistically stationary state. The emulsions before segregation can be described by the dimensionless Weber number We_l . Starting from a baseline case (baseline), the gravitational acceleration g for the segregation process is varied. More precisely, g is halved in case low g and doubled in case high g with respect to the baseline case. Furthermore, the surface tension coefficient σ is varied for the cases low σ and high σ , resulting in different droplet size distributions at the statistically stationary state before the segregation. Note that for constant ρ_c and ε , which is the case here, the correlation between d_H and σ reads $d_H = \sigma^{3/5}$; see also Eq. (5). For the variation in σ , the entire emulsification process has been simulated to obtain the respective emulsions at the statistically stationary state. The employed value for the surface tension $\sigma_{BL} = 2 \times 10^{-2} \text{ N/m}$ approximates that of realistic fluids.²¹ The gravitational acceleration $g_{BL} = 4.59 \text{ m/s}^2$ has been chosen to obtain a Bond number $Bo = \Delta\rho g R^2/\sigma$ of Hinze droplets comparable to the realistic examples of liquid-liquid emulsions (estimated values $\Delta\rho = 100 \text{ kg/m}^3$, $g = 9.81 \text{ m/s}^2$, $R = 1.6 \times 10^{-3} \text{ m}$, and $\sigma = 2 \times 10^{-2} \text{ N/m}$). Additionally, it is worth noting that for gravity-driven rising/falling of a dispersed phase, the ratio of the density difference to the density of the disperse phase $\Delta\rho/\rho_d$ is decisive, and the ratio in our simulations corresponds to that of realistic liquid-liquid emulsions.

To monitor the segregation progress, we track the interface area A and the center of mass of each phase h_i . The interface area of the

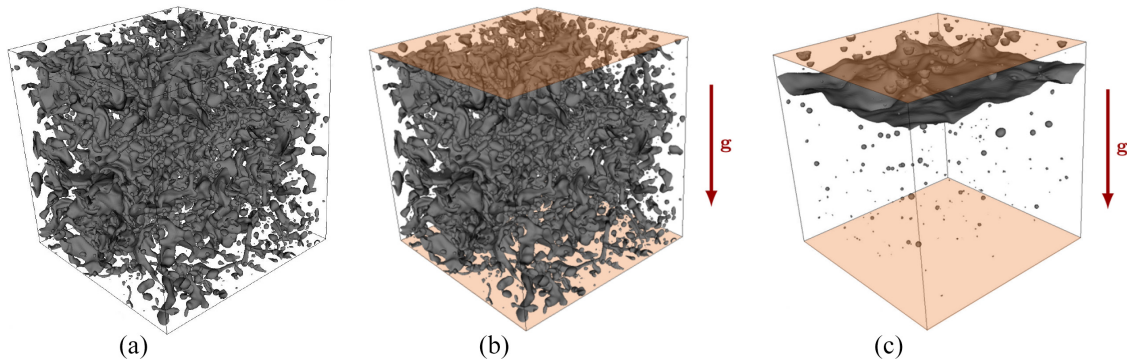


FIG. 1. Simulation setup. (a) Turbulent emulsion at statistically stationary state, (b) forcing is turned off, the gravitational acceleration g is activated, and slip walls are prescribed in the direction of the gravitational acceleration (orange walls), and (c) segregation under g .

dispersed phase is numerically approximated with the volume integral of the gradient of the VOF marker function $|\nabla\alpha|$. As reference for the interface area, the theoretically completely segregated state with $A_\infty = L^2$ is used.

IV. RESULTS

We first study the segregation process for varying g and σ based on the obtained simulation results (Sec. IV A). In Secs. IV B and IV C, we analyze the segregation process from the perspective of the energy releases driving it. At the end of this section (Sec. IV D), we derive correlations to estimate the characteristic velocity and the timescale of the segregation process.

A. Effect of g and σ

Figure 2 visualizes the segregation for different gravitational accelerations g , while Fig. 3 shows the same process for emulsions with different surface tension coefficients σ . In Fig. 2 (variation in g), a difference in the segregation progress can already be seen at the second time step visualized [see Fig. 2(ii)]. At a higher g , a larger fraction of the lighter phase has risen, and fewer dispersed structures are visible in the lower part of the box. As time progresses, the faster segregation at higher g becomes more evident. Finally, at the last time step shown [see Fig. 2(iv)], a clear difference for different g can be seen. At the highest g [see Fig. 2(c-iv)], only a few very small structures are visible in the lower part. Furthermore, it should be noted that in all

configurations (a)–(d), some structures of the heavier phase are enclosed at the upper boarder, resulting in the interfaces visible there.

Figure 3 illustrates the segregation for different σ . Here, the distribution of the dispersed phase in the emulsion differs significantly. The higher the surface tension coefficient, the larger are the structures of the dispersed fluid. For the case low σ [see Fig. 3(a)], there are many small structures with a smaller buoyancy force, which is proportional to $\Delta\rho V$, higher drag forces as well as more interactions in between the dispersed structures. For these reasons, the segregation progress at lower σ is significantly slower than for the cases with a higher σ . At the highest σ [see Fig. 3(c)], comparably large structures are present, and they experience a higher buoyancy force than smaller structures. Additionally, the high σ promotes coalescence even more. For the high σ case, a nearly complete segregation is reached at the last time step visualized [see Fig. 3(c-iv)].

Moreover, the time series in Figs. 2 and 3 also illustrate the different droplet shapes during the segregation process. As expected, small droplets have a quasi-spherical shape due to the dominance of the surface tension forces, while the larger droplets are rather ellipsoidal. Figure 3 shows the effect of the surface tension coefficient on the droplet shapes at comparable size. Comparing the last time steps of the low σ and the baseline case [Figs. 3(a-iv) and 3(b-iv)], it can be seen that droplets of comparable size are more ellipsoidal for the low σ case. Regarding the droplet shape, there is an interplay between the surface tension force, which aims at a spherical shape, gravity, which affects the buoyancy force and also the hydrodynamic pressure inside the droplet, and the turbulent flow field. The well-known Grace-Diagram⁵⁵ allows for estimations of drop and bubble shapes as a function of the Eötvös number, also known as the Bond number, and the bubble Reynolds number. The Eötvös/Bond number and its significance will be discussed in more detail in Sec. IV B.

The segregation process under gravity can be characterized by the height of each phase and the interface area. In process engineering, mostly the height of the lighter phase or a coalescence or creaming interface is used to quantify the segregation; see, e.g., Aleem *et al.*¹⁹ These quantities are optically easily accessible and are, therefore, commonly used. Note that the height refers to the position in the direction of the gravitational acceleration. In Fig. 4, we have tried to adopt the experimental procedure for characterizing the segregation to our simulation results and have in particular, post-processed them for this

TABLE II. Considered cases. The baseline values (BL) are $\sigma_{BL} = 2 \times 10^{-2}$ N/m, $d_{HBL} = 0.1468$ m, and $g_{BL} = 4.59$ m/s². Note that the correlation between d_H and σ for constant ρ_c and ε reads $d_H = \sigma^{3/5}$; see also Eq. (5). The last three columns contain the dimensionless segregation number Seg , the dimensionless energy release ratio Ψ , and the ratio Seg/Ψ ; see Sec. IV B for details.

Case	We_l	σ/σ_{BL}	d_H/d_{HBL}	g/g_{BL}	Seg	Ψ	Seg/Ψ
Baseline	21	1.0	1.00	1.0	10.6	2.5	4.2
Low g	21	1.0	1.00	0.5	5.3	1.3	4.2
High g	21	1.0	1.00	2.0	21.2	5.0	4.2
Low σ	70	0.3	0.49	1.0	18.3	4.6	4.0
High σ	4	5.0	2.63	1.0	5.6	1.8	3.2

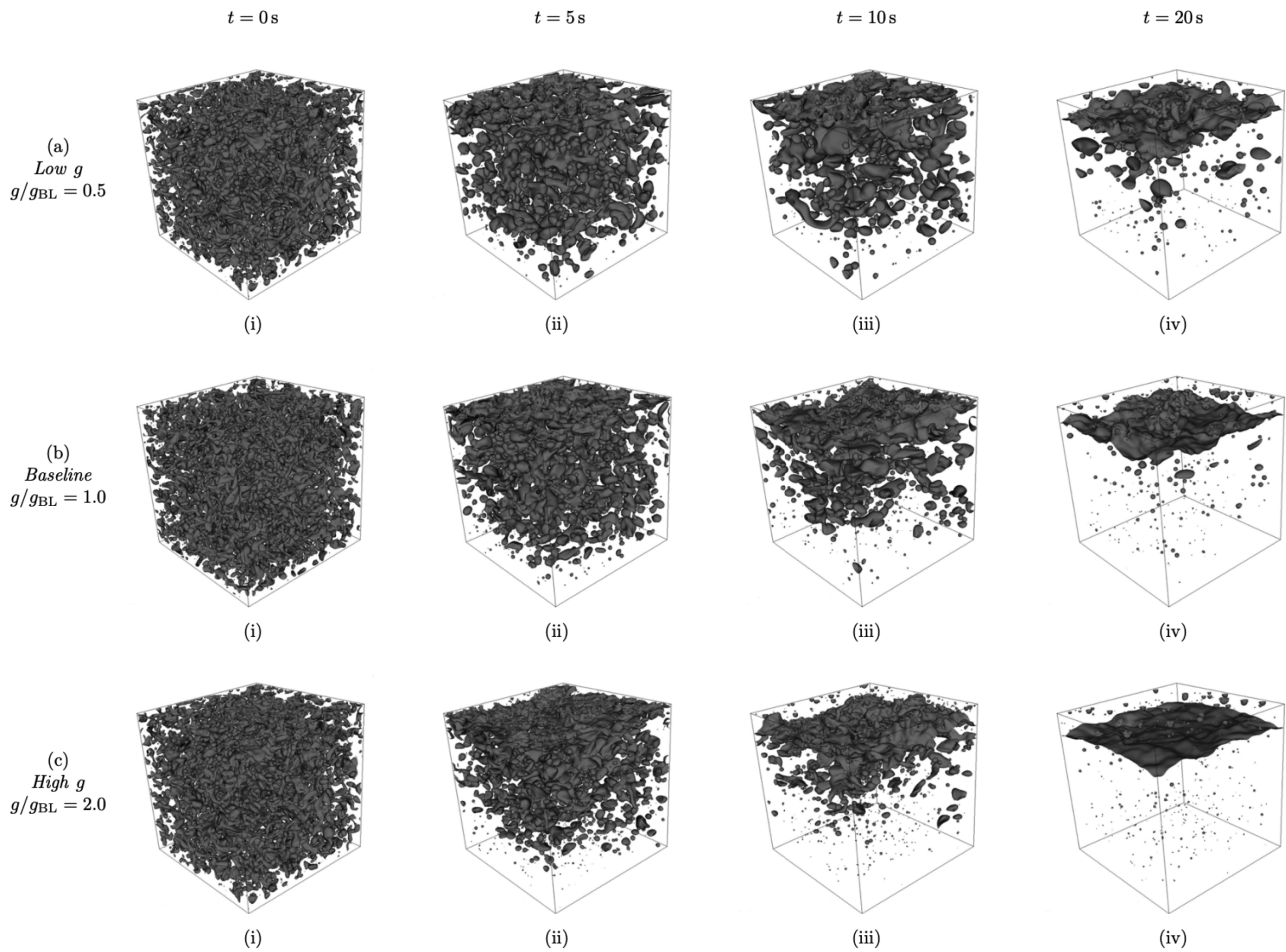


FIG. 2. Visualization of the segregation process for varying g . Rows correspond to different g values with (a) low g , (b) baseline, (c) high g , and columns to different time instants (i), (ii), (iii), and (iv) ($t = \{0, 5, 10, 20\}$ s). The images show the iso-surface of the volume fraction corresponding to $\alpha = 0.5$.

purpose. Furthermore, for a more accurate evaluation, we have monitored the height of the center of mass of each phase during our simulations. As can be seen in Figs. 4(b) and 4(c), the monitored height of the center of mass matches the optical impression. In a bounded domain, the changes of height are directly coupled by the correlation $\Delta h_c = -\phi/(1 - \phi)\Delta h_d$ [see also Eq. (9)], which can be seen in the visualization in Fig. 4. In the following, we present only the height of the center of mass of the dispersed phase, where the change is more evident.

Figure 5 visualizes the segregation progress measured by the height (a) and (b) and the interface area (c) and (d). The left columns (a) and (c) depict the data for different gravity accelerations, and the right columns (b) and (d) illustrate the progress in different surface tension coefficients. As discussed above, a stronger gravitational force promotes the segregation and leads to a faster change in the heights of the center of mass. The surface tension coefficient also alters the segregation progress, since a higher surface tension coefficient accelerates the segregation measured as the height of the lighter phase. As can be seen in Fig. 3, larger droplets are present for higher surface tension

coefficients, and the coalescence process is faster, which enhances the rise of the lighter phase. Additionally, the interface area can also be considered to characterize the segregation progress. For the present configuration, the recorded data are shown in Figs. 5(c) and 5(d). It has to be noted that due to the upper and lower bounds in our configuration, structures must coalesce at a certain point in time, and, thus, the final coalescence process is clearly dominated by the gravitational acceleration. Figure 5(c) reveals that after about $t = 7$ s, the segregation measured by the interface area is predominantly governed by the gravitational acceleration. Before that ($t < 7$ s), a smaller g leads to a somewhat faster decay of the interface area; see Fig. 5(c). We explain this by the fact that at a lower g , the structures remain at the same height a little longer and, thus, have more time to coalesce. For the evolution of the relative interface area A/A_{em} at varying σ [Fig. 5(d)], no clear trend can be observed. It should be noted that the interface area of the emulsion A_{em} is significantly larger for smaller surface tension coefficients, which biases the representation. The time derivative $\partial A/\partial t$, or more precisely that of the surface tension energy $\sigma\partial A/\partial t$, is more suitable for a comparison and will be analyzed in Sec. IV C.

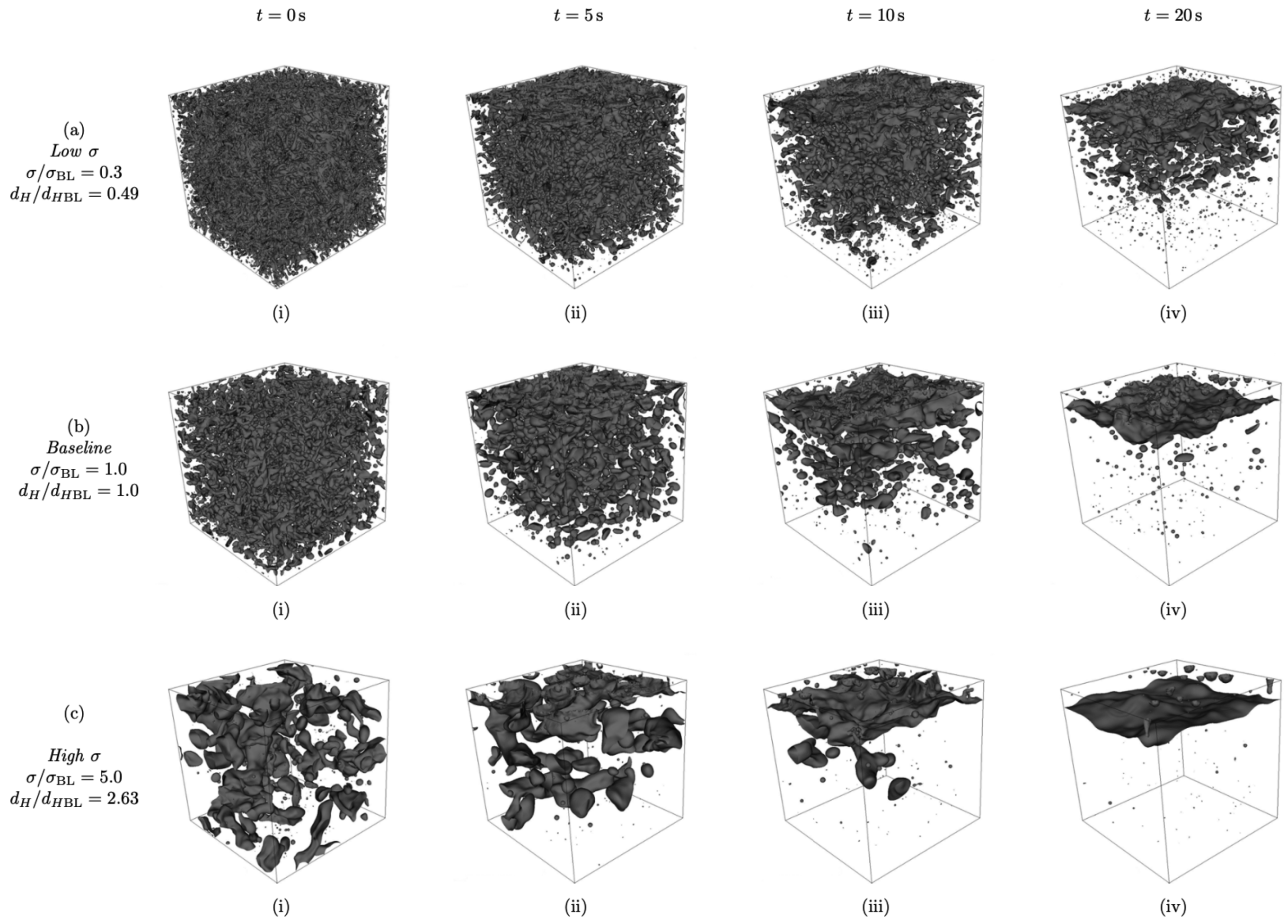


FIG. 3. Visualization of the segregation process for varying σ . Rows correspond to different σ values with (a) low σ , (b) baseline, (c) high σ , and columns to different time instants (i), (ii), (iii), and (iv) ($t = \{0, 5, 10, 20\}$ s). The images show the iso-surface of the volume fraction corresponding to $\alpha = 0.5$.

Furthermore, the strongly fluctuating evolution at the *High* σ case is related to the smaller number of droplets present in this configuration.

Overall, we conclude that for the present configuration, a clear correlation for the evolution of the interface can be expected only when there is no gravitational effect. The comparison of the evolution of the height and the interface area demonstrates that for the configurations studied, the height is more representative of the segregation progress and is, therefore, considered in the following.

B. Driving mechanisms and dimensionless segregation number

Without energy input, the emulsions are unstable and segregate over time as visualized in Sec. IV A. The segregation is driven by the energy release due to the minimization of the net potential energy and that of the surface energy. The change of the potential energy of a two phase flow composed of a carrier and dispersed phase is given by the following equation:

$$\Delta E_{pot} = (\rho_c V_c \Delta h_c + \rho_d V_d \Delta h_d)g. \quad (8)$$

In a bounded domain, the change of heights is restricted to $V_c \Delta h_c + V_d \Delta h_d = 0$. Using this and $V_d = \phi V$, $V_c = (1 - \phi)V$, the relation

$$\Delta h_c = -\frac{\phi}{1-\phi} \Delta h_d \quad (9)$$

is obtained. Thus, Eq. (8) can be simplified to

$$\Delta E_{pot} = -\Delta \rho g V_d \Delta h_d, \quad (10)$$

with $\Delta \rho = \rho_c - \rho_d$, which is in the considered configuration positive since $\rho_c > \rho_d$. Consequently, the rise of the lighter phase (here, the dispersed phase) releases energy ($\Delta E_{pot} < 0$).

The change of the surface energy is given by

$$\Delta E_\sigma = \sigma \Delta A. \quad (11)$$

Breakup leads to an increase in the interface area ($\Delta A > 0$) and requires energy input, while coalescence leads to a reduction in the interface area ($\Delta A < 0$), thus releasing energy ($\Delta E_\sigma < 0$).

To identify the dominant mechanism promoting the segregation, we propose a non-dimensional energy release ratio Ψ of these two driving mechanisms

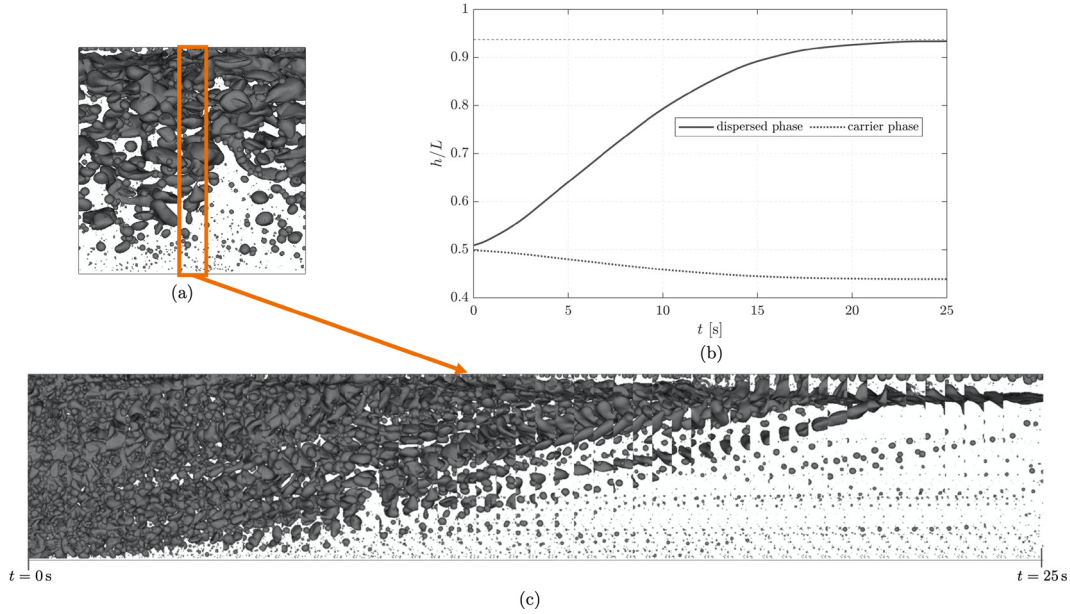


FIG. 4. Visualization of the segregation process. (a) Front view on the emulsion, (b) recorded evolution of the center of mass of the dispersed and carrier phase, and (c) time series of the orange section highlighted in (a) at a frame rate of 2 frames/s.

$$\Psi = \frac{\Delta E_{pot}}{\Delta E_{\sigma}} = \frac{-\Delta \rho g V_d \Delta h_d}{\sigma \Delta A}. \quad (12)$$

The above correlation depends on several case specific quantities, such as V_d , Δh_d , and ΔA , where especially the latter is often *a priori* unknown. In the following, we aim to derive a dimensionless correlation, which depends only on the fluid properties $\Delta \rho$ and σ , the gravitational acceleration g , and two characteristic length scales— d for a representative droplet size and H for a representative length scale of the segregation progress. To this end, we substitute the change of the interface area $\Delta A = A_{\infty} - A_{em}$, where A_{∞} is the interface area at a fully segregated state, and A_{em} is the interface area of the emulsion at the stationary state, by $\Delta A \approx -A_{em}$, which is valid for $A_{\infty} \ll A_{em}$. Furthermore, A_{em} can be expressed with the Sauter mean diameter $d_{32} = 6V_d/A_{em}$, for which constant relations to the Hinze scale have been reported $d_{32} \propto d_H$.^{56–58} This allows for the approximation

$$\Delta A \approx -6V_d/d_{32}. \quad (13)$$

Additionally, substituting Δh_d with a representative length scale H gives

$$\Psi \approx \frac{1}{6} \frac{\Delta \rho g d_{32} H}{\sigma}. \quad (14)$$

Using this correlation, a dimensionless segregation number Seg can be defined as

$$Seg = \frac{\Delta \rho g d H}{\sigma}, \quad (15)$$

where the representative length scale for the segregation process H is the height the lighter (here, the dispersed) phase rises on average. In a bounded domain with length L , H can be calculated using

$H = (1 - 0.5\phi)L - 0.5L = 0.5(1 - \phi)L$, which here is $H = 7/8\pi$. d stands for a representative diameter of the emulsion, which can be approximated with d_{32} or d_H . It is worth noting that the dimensionless segregation number Seg closely resembles the dimensionless Bond number Bo , also known as Eötvös number, with

$$Bo = \frac{\Delta \rho g R^2}{\sigma}, \quad (16)$$

for rising/falling bubbles or droplets with radius R . However, Bo has a different physical relevance since it describes the ratio of body forces to surface forces and characterizes the bubble/droplet shape and the tendency for a breakup. R in Eq. (16) can be substituted by a different characteristic length scale of the bubble/droplet. Because of their different physical meanings, Seg and Bo use different length scales. The length scale for Bo is associated with the bubble/droplet, while for Seg , the product of a length scale associated with the bubble/droplet (denoted here by d) and one associated with the segregation process (denoted here by H) is used. Note that a Bond number Bo with a characteristic length scale of \sqrt{dH} , which is physically difficult to motivate, leads to the same expression as Seg .

Table II contains the segregation number Seg determined with d_H together with the dimensionless energy release ratio Ψ evaluated using the changes between $t = 0$ s and $t = 25$ s. A higher Seg (or higher Ψ) indicates that the release of the potential energy dominates for segregation, while a lower number implies a more important role of the surface tension energy release. It should be noted that the segregation number Seg (or Ψ) indicates only the ratio of the two energy releases and does not provide any information about the timescale of the segregation process, which is analyzed in Sec. IV D.

The ratio Seg/Ψ is also included in Table II. For a variation in g , the ratio is a constant confirming the validity of the above made

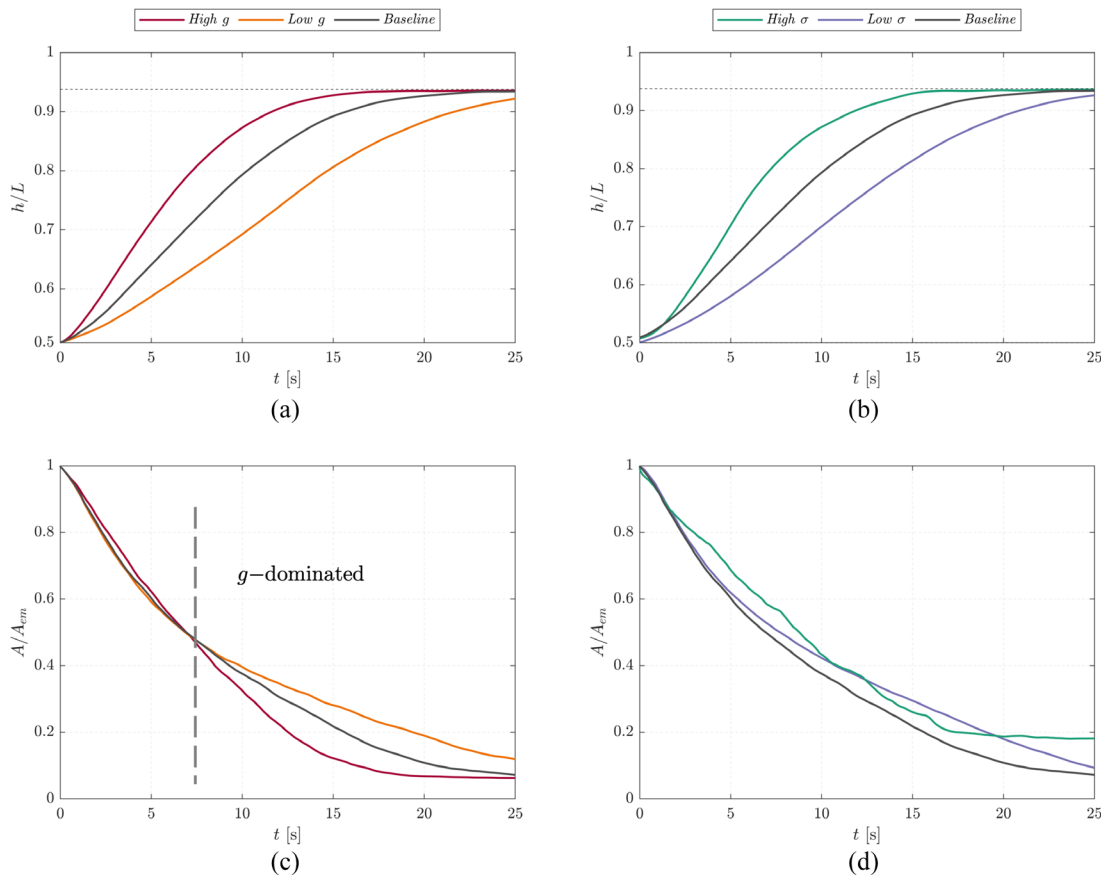


FIG. 5. Segregation progress measured by the height of the center of mass of the dispersed phase (a) and (b) and the interface area (c) and (d). The effect of different gravitational forces is shown in (a) and (c), whereas the effect of different surface tension coefficients is illustrated in (b) and (d).

approximations. When σ is varied, the ratio is approximately the same, but the values scatter. We conjecture that this is due to the approximation used for ΔA [Eq. (13)].

C. Energy release rates and decay of turbulent kinetic energy

For the actual segregation, not only the amount of the energy release but also the time over which it is released is crucial. To this end, we propose to evaluate the energy release rates. Using Eqs. (10) and (11), the energy release rates are as follows:

$$\dot{E}_{pot} = \Delta\rho V_d \dot{h}_d g, \quad \dot{E}_\sigma = \sigma \dot{A}. \quad (17)$$

As discussed above, during the segregation progress, both quantities are negative and therewith drive this process. Figure 6 visualizes the energy release rates. For the variation in the gravitational acceleration [Fig. 6(a)], the energy release for the potential energy \dot{E}_{pot} clearly increases with increasing g , while the energy release due to the reduction in the surface energy \dot{E}_σ is similar for the three g -variations; see Fig. 6(a). The difference between \dot{E}_{pot} at different g is not only caused by the different g values, but also the resulting different \dot{h} , amplifying the differences in the energy release. The variation in the surface

tension coefficient [see Fig. 6(b)] does not reveal such a clear trend. As expected, the energy release from the surface tension term \dot{E}_σ increases with increasing σ ; however, the value of σ also affects the release of the potential energy \dot{E}_{pot} . At a smaller σ , the dispersed phase remains in a more disturbed state, i.e., smaller droplets, for a longer time. This leads to a greater number of droplet interactions and mutual hindering effects, limiting the rise of the lighter phase and, thus, the release of the potential energy. Conversely, a higher σ means fewer droplets as well as faster coalescence and, consequently, less restriction on the release of the potential energy. Hence, the release of the potential energy appears to scale proportional to the droplet size in the emulsions; see also Fig. 6(b).

Furthermore, the release of the potential and surface energy affects the decay of the turbulent kinetic energy, which is depicted in Fig. 7. Figure 7(a) shows that a higher g results in higher energy release due to the decreasing potential energy, which is transformed in the kinetic energy and retards the decay of the latter. The variation in σ also affects the decay of the turbulent kinetic energy [Fig. 7(b)]. However, due to the complex interplay of droplet size distributions and the release of the gravitational energy, no clear trend is observed. For a detailed study of the effect of varying σ on the decay of the turbulent kinetic energy in decaying

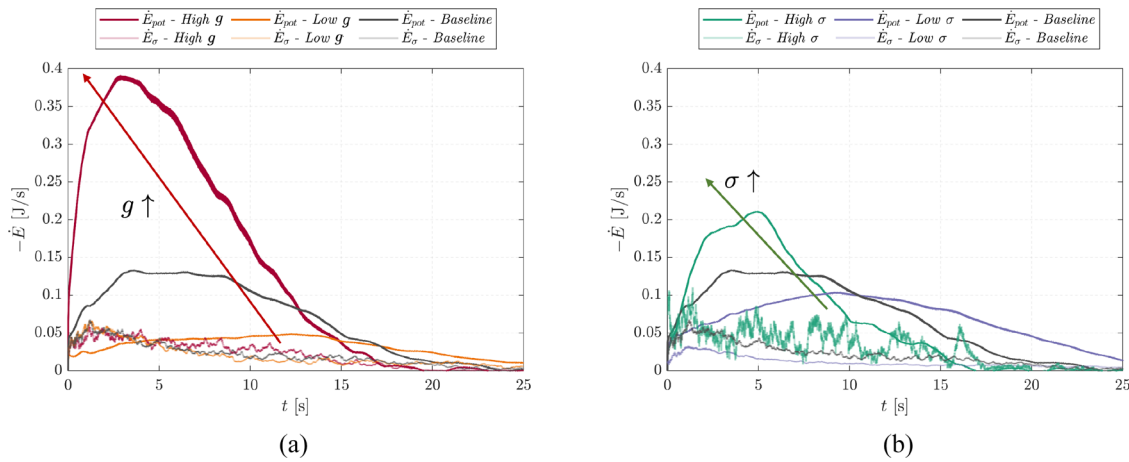


FIG. 6. Energy release rates due to the reduction in the net potential height \dot{E}_{pot} and the reduction in the interface area \dot{E}_{σ} for varying g in (a) and varying σ in (b).

turbulence without gravitational force, we refer the reader to Dodd and Ferrante.²⁹

D. Timescale of the segregation process

For practical applications, the duration of the segregation process and the effects of parameter changes on this duration are of particular interest. Therefore, we attempt to derive a characteristic timescale for segregation progress. For this purpose, we consider the time evolution of the height of the lighter phase and its time derivative that represents an average rising velocity.

Figures 8(a) and 8(b) illustrate the temporal derivative of the height of the center of mass of the dispersed phase \dot{h}_d . As discussed in Subsection IV C, in the case of a variation in g , \dot{h}_d clearly increases for an increasing g ; see Fig. 8(a). The droplet size distribution (associated with σ) alters the release rate of the potential energy and, thus, \dot{h}_d . A more dispersed emulsion, characterized by a smaller d_H , has a higher hindering effect and limits the release of the potential energy, whereas a less dispersed emulsion, characterized by a higher d_H , allows for a

higher energy release of the potential energy. Consequently, \dot{h}_d increases with increasing σ (increasing d_H), see Fig. 8(b).

The average rising velocity of a single droplet due to gravitational acceleration, neglecting friction forces, is given by

$$U_g = \frac{H}{t} = \sqrt{\frac{1}{2} \frac{\Delta\rho}{\rho_d} gH}, \quad (18)$$

where H stands for the height, which the dispersed phase has risen. The detailed derivation of this relation is provided in the Appendix. This velocity, of course, significantly overestimates the average rising velocity of the considered configuration as the friction forces and droplet–droplet interactions are neglected. However, the gravity-based velocity [Eq. (18)], together with the observations described above, motivate the formulation

$$\dot{h}_d \propto U_g \xi(d), \quad (19)$$

where \dot{h}_d is assumed to be proportional to a gravity-based velocity U_g and a factor ξ depending on the droplet size distribution of the

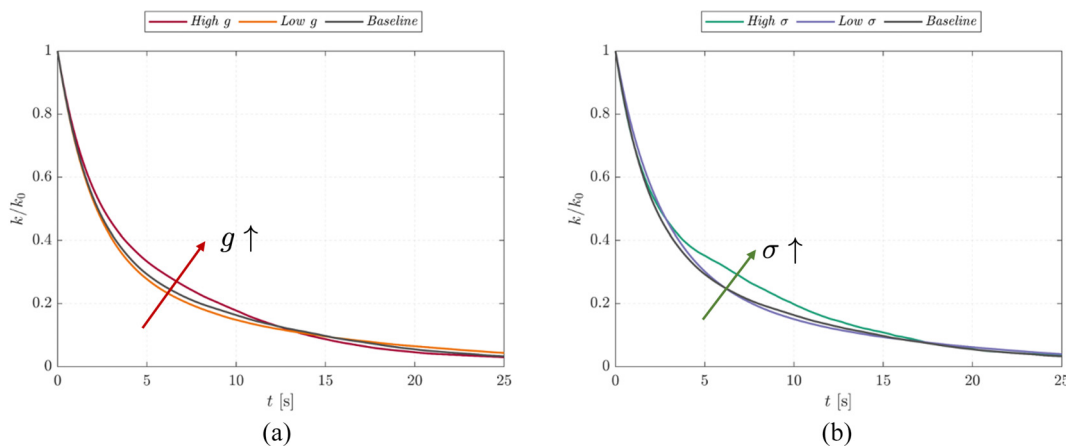


FIG. 7. Decay of the normalized kinetic energy in different configurations for varying g in (a) and for varying σ in (b).

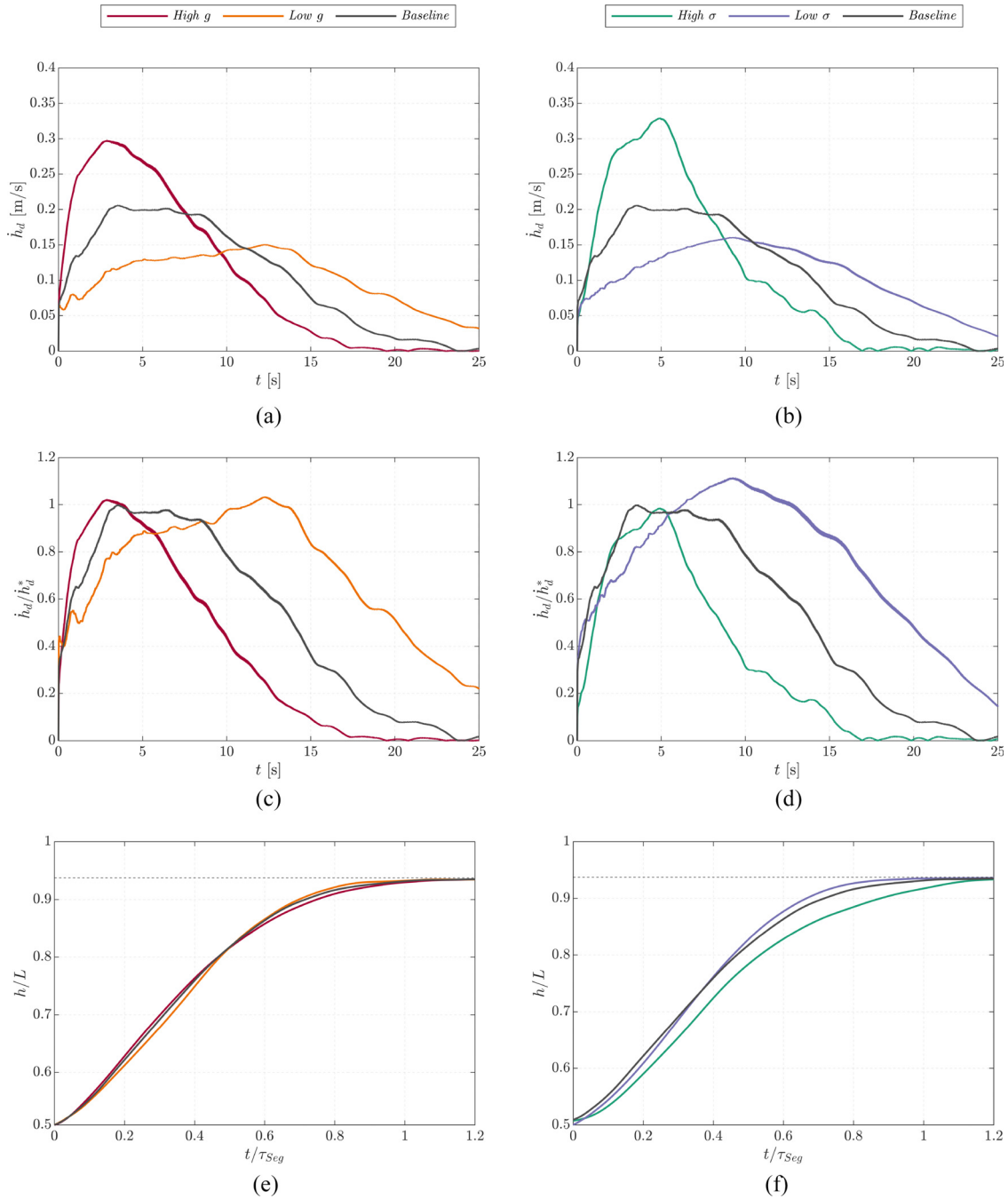


FIG. 8. Temporal derivative of the center of mass of the dispersed phase \dot{h}_d (a) and (b), normalized temporal derivative \dot{h}_d/\dot{h}_d^* (c) and (d), and the temporal evolution of h/L scaled by the proposed timescale (e) and (f). The left columns (a), (c), and (e) show these quantities for different gravitational accelerations g , and the right columns (b), (d), and (f) illustrate them for different surface tension coefficients σ .

emulsion. The proposed relation is a simplification for the configurations considered here. For other configurations, additional effects of other parameters, such as viscosity, would also have to be incorporated. We approximate d with the Hinze scale d_H and propose

$$\zeta = (d_H/d_{ref})^\gamma. \quad (20)$$

For the considered configuration, we have fitted $\gamma = 0.5$ and for simplicity taken $d_{ref} = d_{HBL}$. This results in the correlation

$$\dot{h}_d^* = c_p U_g \zeta(d) = c_p \sqrt{\frac{1}{2} \frac{\Delta \rho}{\rho_d} g H} \sqrt{\frac{d_H}{d_{ref}}} \quad (21)$$

where c_p denotes a proportionality factor depending on the choice of d_{ref} . For $d_{ref} = d_{HBL}^*$, c_p is fitted to $c_p = 0.25$. The measured velocities \dot{h}_d normalized by \dot{h}_d^* [Eq. (21)] are plotted in Figs. 8(c) and 8(d). In all cases, the normalized velocities have their maximum at about 1, which confirms the validity of the approximations made.

Furthermore, the derived correlation allows for an estimation of a timescale for the segregation. Using Eqs. (19) and (20), the following is obtained:

$$\tau_{Seg} \propto \frac{H}{U_g (d_H/d_{ref})^\gamma} \quad (22)$$

Using, additionally, the definition of U_g [Eq. (18)] results in

$$\tau_{Seg} \propto \sqrt{\frac{\rho_d H}{\Delta \rho g}} \left(\frac{d_{ref}}{d_H}\right)^\gamma \quad (23)$$

Thus, for a variation in only g , the timescale is proportional to $\tau \propto 1/\sqrt{g}$, and for a variation in only the droplet size distribution (σ), the timescale is proportional to $\tau \propto 1/d_H^\gamma$.

For the considered configuration, the timescale of the segregation can be explicitly calculated as

$$\tau_{Seg} = \frac{H}{c_p U_g (d_H/d_{ref})^\gamma} \quad (24)$$

Using $\gamma = 0.5$, $c_p = 0.25$, and Eq. (A5) gives

$$\tau_{Seg} = 2^{5/2} \sqrt{\frac{\rho_d H}{\Delta \rho g}} \sqrt{\frac{d_{ref}}{d_H}} \quad (25)$$

where $H = 7/8\pi$. Figures 8(e) and 8(f) show the height of the dispersed phase h plotted over the time normalized by the characteristic timescale. It can be seen that for both variations, the segregation measured by height is completed at τ_{Seg} . Moreover, it is noteworthy that the scaled temporal evolution of the heights almost coincides to one line when g is varied, see Fig. 8(e).

V. CONCLUSIONS

In this work, we have numerically studied the segregation of turbulent emulsions under different gravitational accelerations g and with different droplet size distributions obtained by altering the surface tension coefficient σ . To this end, we first generated turbulent emulsions in a linearly forced HIT and then turned off the forcing and activated the gravitational acceleration. This approach enabled us to study the segregation process using well-defined initial conditions. To our knowledge, this work represents the first numerical investigation of the gravity-driven segregation process. With it, we extend previous numerical studies focusing on emulsification or emulsions at the statistically stationary state. Moreover, the time-resolved, three-dimensional visualization of the segregation progress obtained by our DNS studies supplements the existing experimental studies on segregation. We have approached this topic from the thermodynamic perspective of energy releases, adding an important complementary perspective to this physical process.

Segregation can be quantified by the height of each phase and the interface area. In this study, we have primarily analyzed the temporal evolution of the height of the dispersed phase. Moreover, we have addressed the energy release of the two central processes, namely, the rise of the lighter phase (release of the potential energy) and coalescence (release of the surface energy). Based on our observations, we have defined a dimensionless segregation number Seg that characterizes the ratio of the potential energy release to the surface energy release, allowing for an identification of the dominating process. In addition, we evaluated and compared the energy release rates. Our simulation results show that a smaller droplet size, i.e., smaller σ , hinders and limits the release of the potential energy.

Finally, we have derived a correlation to estimate the average rising velocity of the lighter phase, which also allows for the derivation of a characteristic timescale. We found that the average rising velocity is a fraction of a gravity-based velocity and depends on the size of the droplets in the emulsion. Scaling of the velocities and the time with the empirically derived correlation showed good agreement.

The presented work can be considered as a first important step toward the numerical assessment of emulsion segregation. The subject of the current investigations is the evaluation of droplet size distributions during the segregation process. Therefore, in order to obtain statistically reliable data, a multitude of identical segregation processes have to be simulated simultaneously. Furthermore, in future studies, we plan to consider configurations with varying density differences between the dispersed and carrier phase to assess the effect of the density difference on the segregation and its timescale.

ACKNOWLEDGMENTS

This project received funding by *dtec.bw*—Digitalization and Technology Research Center of the Bundeswehr—under the project *MORE*, which is gratefully acknowledged. Furthermore, the authors thank the Gauss Centre for Supercomputing e.V. (www.gauss-centre.eu) for funding this project by providing computing time on the GCS Supercomputer SuperMUC-NG at the Leibniz Supercomputing Centre (www.lrz.de).

AUTHOR DECLARATIONS

Conflict of Interest

The authors have no conflicts to disclose.

Author Contributions

Theresa Trummler: Conceptualization (lead); Formal analysis (lead); Investigation (equal); Resources (equal); Supervision (lead); Writing – original draft (lead); Writing – review & editing (lead). **Alexander Begemann:** Conceptualization (supporting); Data curation (lead); Investigation (lead); Methodology (equal); Software (equal); Validation (lead); Visualization (lead). **Elias Trautner:** Conceptualization (supporting); Investigation (supporting); Methodology (equal); Software (equal); Supervision (supporting); Validation (supporting); Visualization (supporting); Writing – original draft (supporting); Writing – review & editing (supporting). **Markus Klein:** Project administration (lead); Resources (lead); Writing – original draft (supporting); Writing – review & editing (supporting).

DATA AVAILABILITY

The data that support the findings of this study are available from the corresponding author upon reasonable request.

APPENDIX: A DETAILED DERIVATION OF THE RELATION FOR THE GRAVITY-BASED CHARACTERISTIC VELOCITY U_g

1. Gravity-based velocity derived from the force balance on a droplet

A gravity-based characteristic velocity U_g can be derived based on the force balance on a droplet with mass m ($m = \rho_d V_{droplet}$). Neglecting friction forces and other losses, the force balance reads

$$m_d \ddot{x} = F_b - F_g, \tag{A1}$$

where F_b denotes the buoyancy force with $F_b = \rho_c V_{droplet} g$, and F_g denotes the gravitation force with $F_g = \rho_d V_{droplet} g$. This leads to the following acceleration:

$$\ddot{x} = \frac{\Delta\rho}{\rho_d} g. \tag{A2}$$

Integrating twice in time and using the initial conditions $\dot{x} = 0$, $x = 0$ gives

$$x = \frac{\Delta\rho}{\rho_d} g \frac{1}{2} t^2. \tag{A3}$$

The distance over a time t is set to $x = H$, and t can be expressed as follows:

$$t = \sqrt{2 \frac{\rho_d H}{\Delta\rho g}}. \tag{A4}$$

Thus, the average velocity resulting from gravitation over a distance H can be determined with

$$U_g = \frac{H}{t} = \sqrt{\frac{1}{2} \frac{\Delta\rho}{\rho_d} g H}. \tag{A5}$$

This relation can alternatively be derived by evaluating the velocity based on the kinetic energy equivalent of the release of the potential energy, as shown below.

2. Gravity-based velocity derived from the energy release of the potential energy

The gravity-based characteristic velocity [Eq. (A5)] can also be derived by evaluating the velocity based on the kinetic energy equivalent of the release of the potential energy. For consistency, we also consider the kinetic energy in the carrier phase. This gives the following balance:

$$\frac{1}{2} \rho_d V_d U_{g,max}^2 + \frac{1}{2} \rho_c V_c U_{c,g,max}^2 = -\Delta E_{pot}, \tag{A6}$$

where $U_{g,max}$ refers to the maximum velocity in the dispersed phase to be consistent with the nomenclature used so far and $U_{c,g,max}$ to that in the carrier phase. Using Eq. (9), we can recast the left part to

$$\frac{1}{2} \rho_d V_d U_{g,max}^2 \left(1 + \frac{\rho_c \phi}{\rho_d (1-\phi)} \right) = -\Delta E_{pot}. \tag{A7}$$

We simplify this expression with $\beta = \frac{\rho_c \phi}{\rho_d (1-\phi)}$. Note that for small void fractions and density ratios close to 1, this expression vanishes ($\beta \rightarrow 0$). Inserting the expression for the release of the potential energy from Eq. (10) yields

$$\frac{1}{2} \rho_d V_d U_{g,max}^2 (1 + \beta) = \Delta\rho V_d g \Delta h_d. \tag{A8}$$

Based on this correlation, we can derive a maximum velocity associated with the energy release of the potential energy that reads

$$U_{g,max} = \sqrt{\frac{2}{1 + \beta} \frac{\Delta\rho}{\rho_d} g \Delta h_d}. \tag{A9}$$

Assuming that the initial velocity is zero and the acceleration is linear, the average velocity can be approximated by $U_g \approx \frac{1}{2} U_{g,max}$. Furthermore, we substitute Δh_d with H and obtain

$$U_g = \sqrt{\frac{1}{2(1 + \beta)} \frac{\Delta\rho}{\rho_d} g H}. \tag{A10}$$

For $\beta = 0$, this expression is identical to Eq. (A5). In the considered configurations, we have $\beta = 0.1587$, which corresponds to a prefactor of $\sqrt{1/(1 + \beta)} = 0.9289$ for U_g and has been neglected in the evaluations shown in the paper for the sake of simplicity.

REFERENCES

- ¹R. Walker, E. A. Decker, and D. J. McClements, "Development of food-grade nano-emulsions and emulsions for delivery of omega-3 fatty acids: Opportunities and obstacles in the food industry," *Food Funct.* **6**, 41–54 (2015).
- ²R. Zhang, Z. Zhang, H. Zhang, E. A. Decker, and D. J. McClements, "Influence of emulsifier type on gastrointestinal fate of oil-in-water emulsions containing anionic dietary fiber (pectin)," *Food Hydrocolloids* **45**, 175–185 (2015).
- ³D. Guzey and D. J. McClements, "Formation, stability and properties of multi-layer emulsions for application in the food industry," *Adv. Colloid Interface Sci.* **128–130**, 227–248 (2006).
- ⁴A. Spornath and A. Aserin, "Microemulsions as carriers for drugs and nutraceuticals," *Adv. Colloid Interface Sci.* **128–130**, 47–64 (2006).
- ⁵C. Dicharry, D. Arla, A. Siquin, A. Graciaa, and P. Bouriat, "Stability of water/crude oil emulsions based on interfacial dilatational rheology," *J. Colloid Interface Sci.* **297**, 785–791 (2006).
- ⁶V. Angardi, A. Etehad, and Ö. Yücel, "Critical review of emulsion stability and characterization techniques in oil processing," *J. Energy Resour. Technol.* **144**, 040801 (2022).
- ⁷F. Hoppe, M. Thewes, J. Seibel, A. Balazs, and J. Scharf, "Evaluation of the potential of water injection for gasoline engines," *SAE Int. J. Engines* **10**, 2500–2512 (2017).
- ⁸C. Heinrich, H. Dörksen, A. Esch, and K. Krämer, "Gasoline water direct injection (GWDI) as a key feature for future gasoline engines," in *International Conference on Knocking in Gasoline Engines* (Springer, 2017), pp. 322–337.
- ⁹M. Chmielewski, P. Niszczota, and M. Gieras, "Combustion efficiency of fuel-water emulsion in a small gas turbine," *Energy* **211**, 118961 (2020).
- ¹⁰S. Welscher, M. H. Moradi, A. Vacca, P. Bloch, M. Grill, U. Wagner, M. Bargende, and T. Koch, "A comprehensive evaluation of water injection in the diesel engine," *Int. J. Engine Res.* (published online 2021).
- ¹¹P. K. Kilpatrick, "Water-in-crude oil emulsion stabilization: Review and unanswered questions," *Energy Fuels* **26**, 4017–4026 (2012).
- ¹²F. Goodarzi and S. Zendejboudi, "A comprehensive review on emulsions and emulsion stability in chemical and energy industries," *Can. J. Chem. Eng.* **97**, 281–309 (2019).

- ¹³W. Dalingaros, S. Jeelani, and S. Hartland, "Prediction of steady-state dispersion height in the disengaging section of an extraction column from batch settling data," *Can. J. Chem. Eng.* **65**, 210–213 (1987).
- ¹⁴S. A. K. Jeelani and S. Hartland, "Effect of dispersion properties on the separation of batch liquid-liquid dispersions," *Ind. Eng. Chem. Res.* **37**, 547–554 (1998).
- ¹⁵S. A. K. Jeelani and S. Hartland, "Prediction of steady state dispersion height from batch settling data," *AIChE J.* **31**, 711–720 (1985).
- ¹⁶M. Henschke, L. H. Schlieper, and A. Pfennig, "Determination of a coalescence parameter from batch-settling experiments," *Chem. Eng. J.* **85**, 369–378 (2002).
- ¹⁷S. Jeelani, G. Benoist, K. Joshi, R. Gunde, D. Kellenberger, and E. J. Windhab, "Creaming and aggregation of particles in suspensions," *Colloids Surf., A* **263**, 379–389 (2005).
- ¹⁸L. Lobo, I. Ivanov, and D. Wasan, "Dispersion coalescence: Kinetic stability of creamed dispersions," *AIChE J.* **39**, 322–334 (1993).
- ¹⁹W. Aleem, N. Mellon, J. A. Khan, and H. H. Al-Kayiem, "Experimental investigation and mathematical modeling of oil/water emulsion separation effectiveness containing alkali-surfactant-polymer," *J. Dispersion Sci. Technol.* **42**, 1286–1213 (2021).
- ²⁰T. Frising, C. Noik, and C. Dalmazzone, "The liquid/liquid sedimentation process: From droplet coalescence to technologically enhanced water/oil emulsion gravity separators: A review," *J. Dispersion Sci. Technol.* **27**, 1035–1057 (2006).
- ²¹M. Koege, C. Mull, Y. N. Mishra, S. Will, and L. Zigan, "Characterization of fuel/water mixtures and emulsions with ethanol using laser-induced fluorescence," *Appl. Opt.* **59**, 1136–1144 (2020).
- ²²P. Perlekar, L. Biferale, M. Sbragaglia, S. Srivastava, and F. Toschi, "Droplet size distribution in homogeneous isotropic turbulence," *Phys. Fluids* **24**, 065101 (2012).
- ²³R. Skartlien, E. Sollum, and H. Schumann, "Droplet size distributions in turbulent emulsions: Breakup criteria and surfactant effects from direct numerical simulations," *J. Chem. Phys.* **139**, 174901 (2013).
- ²⁴S. Mukherjee, A. Safdari, O. Shardt, S. Kenjeres, and H. E. A. Van den Akker, "Droplet-turbulence interactions and quasi-equilibrium dynamics in turbulent emulsions," *J. Fluid Mech.* **878**, 221–276 (2019).
- ²⁵M. Crialesi-Esposito, M. E. Rosti, S. Chibbaro, and L. Brandt, "Modulation of homogeneous and isotropic turbulence in emulsions," *J. Fluid Mech.* **940**, A19 (2022).
- ²⁶A. Begemann, T. Trummler, E. Trautner, J. Hasslberger, and M. Klein, "Effect of turbulence intensity and surface tension on the emulsification process and its stationary state—A numerical study," *Can. J. Chem. Eng.* **100**, 3548–3561 (2022).
- ²⁷A. Komrakova, "Single drop breakup in turbulent flow," *Can. J. Chem. Eng.* **97**, 2727–2739 (2019).
- ²⁸C. Shao, K. Luo, Y. Yang, and J. Fan, "Direct numerical simulation of droplet breakup in homogeneous isotropic turbulence: The effect of the Weber number," *Int. J. Multiphase Flow* **107**, 263–274 (2018).
- ²⁹M. S. Dodd and A. Ferrante, "On the interaction of Taylor length scale size droplets and isotropic turbulence," *J. Fluid Mech.* **806**, 356–412 (2016).
- ³⁰F. Bräuer, E. Trautner, J. Hasslberger, P. Cifani, and M. Klein, "Turbulent bubble-laden channel flow of power-law fluids: A direct numerical simulation study," *Fluids* **6**, 40 (2021).
- ³¹E. Trautner, M. Klein, F. Bräuer, and J. Hasslberger, "Conditional and unconditional second-order structure functions in bubbly channel flows of power-law fluids," *Phys. Fluids* **33**, 055121–055132 (2021).
- ³²J. Hasslberger, P. Cifani, N. Chakraborty, and M. Klein, "A direct numerical simulation analysis of coherent structures in bubble-laden channel flows," *J. Fluid Mech.* **905**, A37 (2020).
- ³³R. Meller, F. Schlegel, and M. Klein, "Sub-grid scale modelling and a-posteriori tests with a morphology adaptive multifield two-fluid model considering rising gas bubbles," *Flow, Turbul. Combust.* **108**, 895–922 (2022).
- ³⁴J. Hasslberger, M. Klein, and N. Chakraborty, "Flow topologies in bubble-induced turbulence: A direct numerical simulation analysis," *J. Fluid Mech.* **857**, 270–290 (2018).
- ³⁵M. Saeedipour, S. Vincent, and J.-L. Estivalezes, "Toward a fully resolved volume of fluid simulation of the phase inversion problem," *Acta Mech.* **232**, 2695–2714 (2021).
- ³⁶J.-L. Estivalezes, W. Aniszewski, F. Auguste, Y. Ling, L. Osmar, J.-P. Caltagirone, L. Chirco, A. Pedrono, S. Popinet, A. Berlemont *et al.*, "A phase inversion benchmark for multiscale multiphase flows," *J. Comput. Phys.* **450**, 110810 (2022).
- ³⁷A. M. Al-Ghamdi, C. Noik, C. Dalmazzone, and S. Kokal, "Experimental investigation of emulsion stability in gas/oil separation plants," *SPE J.* **14**, 595–605 (2009).
- ³⁸V. Sazonov, H. Rottengruber, and P. Dragomirov, "Untersuchung der benzin-wasser-emulsion direkteinspritzung zur effizienzsteigerung von ottomotoren," in *11. Tagung Einspritzung und Kraftstoffe* (Springer, 2019), pp. 515–542.
- ³⁹D. J. McClements, "Critical review of techniques and methodologies for characterization of emulsion stability," *Crit. Rev. Food Science Nutr.* **47**, 611–649 (2007).
- ⁴⁰W. Aniszewski, T. Arrufat, M. Crialesi-Esposito, S. Dabiri, D. Fuster, Y. Ling, J. Lu, L. Malan, S. Pal, R. Scardovelli, G. Tryggvason, P. Yecko, and S. Zaleski, "PARallel, Robust, Interface Simulator (PARIS)," *Comput. Phys. Commun.* **263**, 107849 (2021).
- ⁴¹M. Klein, N. Chakraborty, and S. Ketterl, "A comparison of strategies for direct numerical simulation of turbulence chemistry interaction in generic planar turbulent premixed flames," *Flow, Turbul. Combust.* **99**, 955–971 (2017).
- ⁴²J. Hasslberger, S. Ketterl, M. Klein, and N. Chakraborty, "Flow topologies in primary atomization of liquid jets: A direct numerical simulation analysis," *J. Fluid Mech.* **859**, 819–838 (2019).
- ⁴³F. J. Salvador, S. Ruiz, M. Crialesi-Esposito, and I. Blanquer, "Analysis on the effects of turbulent inflow conditions on spray primary atomization in the near-field by direct numerical simulation," *Int. J. Multiphase Flow* **102**, 49–63 (2018).
- ⁴⁴Y. Ling, D. Fuster, S. Zaleski, and G. Tryggvason, "Spray formation in a quasi-planar gas-liquid mixing layer at moderate density ratios: A numerical close-up," *Phys. Rev. Fluids* **2**, 014005 (2017).
- ⁴⁵A. Prosperetti and G. Tryggvason, *Computational Methods for Multiphase Flow* (Cambridge University Press, 2007).
- ⁴⁶C. W. Hirt and B. D. Nichols, "Volume of fluid (VOF) method for the dynamics of free boundaries," *J. Comput. Phys.* **39**, 201–225 (1981).
- ⁴⁷J. U. Brackbill, D. B. Kothe, and C. Zemach, "A continuum method for modeling surface tension," *J. Comput. Phys.* **100**, 335–354 (1992).
- ⁴⁸S. Popinet, "An accurate adaptive solver for surface-tension-driven interfacial flows," *J. Comput. Phys.* **228**, 5838–5866 (2009).
- ⁴⁹B. P. Leonard, "A stable and accurate convective modelling procedure based on quadratic upstream interpolation," *Comput. Methods Appl. Mech. Eng.* **19**, 59–98 (1979).
- ⁵⁰T. S. Lundgren, "Linearly forced isotropic turbulence," in *Center for Turbulence Research Annual Research Briefs* (Center for Turbulence Research, Stanford, 2003), pp. 461–473.
- ⁵¹J. O. Hinze, "Fundamentals of the hydrodynamic mechanism of splitting in dispersion processes," *AIChE J.* **1**, 289–295 (1955).
- ⁵²C. Rosales and C. Meneveau, "Linear forcing in numerical simulations of isotropic turbulence: Physical space implementations and convergence properties," *Phys. Fluids* **17**, 095106 (2005).
- ⁵³P. L. Carroll and G. Blanquart, "A proposed modification to Lundgren's physical space velocity forcing method for isotropic turbulence," *Phys. Fluids* **25**, 105114 (2013).
- ⁵⁴S. B. Pope, *Turbulent Flows* (IOP Publishing, 2001).
- ⁵⁵J. Grace, T. Wairegi, and T. Nguyen, "Shapes and velocities of single drops and bubbles moving freely through immiscible liquids," *Trans. Inst. Chem. Eng.* **54**, 167–173 (1976).
- ⁵⁶A. Pacek, C. Man, and A. Nienow, "On the sauter mean diameter and size distributions in turbulent liquid/liquid dispersions in a stirred vessel," *Chem. Eng. Sci.* **53**, 2005–2011 (1998).
- ⁵⁷L. Yi, F. Toschi, and C. Sun, "Global and local statistics in turbulent emulsions," *J. Fluid Mech.* **912**, A13 (2021).
- ⁵⁸J. A. Boxall, C. A. Koh, E. D. Sloan, A. K. Sum, and D. T. Wu, "Droplet size scaling of water-in-oil emulsions under turbulent flow," *Langmuir* **28**, 104–110 (2012).